A Topography-Aware Eddy Parameterization Improves Warm Water Transport Across the Cape Darnley Continental Slope

Nicolas Dettling[1], Yoshihiro Nakayama[2,3], Vigan Mensah[3], Martin Losch[1]

[1]Alfred Wegener Institute Helmholtz Centre for Polar and Marine Research
[2]Thayer School of Engineering, Dartmouth College, Hanover, NH, USA
[3]Institute of Low Temperature Science, Hokkaido University, Sapporo, Japan

Key Points:

- In a regional ocean model, the downslope flow of dense water in the Cape Darnley region produces an eddy-driven onshore warm water transport
- At coarse resolution, the onshore transport of warm water is absent but can be restored by employing a classical eddy parameterization
- The parameterization is most effective when it is modified to consider the suppressive effect of sloping bottom topography

Corresponding author: Nicolas Dettling, nicolas.dettling@awi.de

Abstract

The onshore transport of warm Circumpolar Deep Water determines the properties of Antarctic shelf waters and drives the melting of the Antarctic ice shelves. The largest net onshore transport of CDW coincides with regions of dense water export, such as the Cape Darnley region in the East Antarctic, one of the major sources of Antarctic Bottom Water. In an eddy-resolving regional ocean model of the Cape Darnley region, the winter downslope flow of dense water produces an eddy-driven transport of warm modified Circumpolar Deep Water across the shelf break. At coarse resolution typical for climate models, this warm water transport is absent and needs to be parameterized. The Gent and McWilliams/Redi (GM/Redi) scheme improves the simulated hydrographic fields and recovers a transport of warm water across the shelf break. With high constant GM/Redi coefficients that improve the mean hydrography the most, however, the on-shelf transport of warm water is overestimated. This is because the dynamical suppression of eddy-driven transports across sloping bottom topography is not considered in the GM/Redi scheme. Therefore, we implement a topography-aware version of the GM/Redi scheme that reduces the coefficients over steep continental slopes, representing the eddy-suppressive effect of sloping bottom topography. The topography-aware GM/Redi scheme outperforms the traditional version by simultaneously improving the mean hydrographic fields and the cross-slope warm water transports. Eddy parameterizations remain important for the representation of onshore tracer transports and shelf water masses in ocean models provided they incorporate regional and local physics as in our example of a topography-aware scheme.

Plain Language Summary

Eddies—ocean whirls with length scales of tens to hundreds of kilometers—transport warm water across the Antarctic continental slope and onto the shelf, where they contribute to the melting of Antarctic ice masses. In a high-resolution regional model of the Cape Darnley region in East Antarctica, eddies form when dense water flows from the shelf into the deep ocean. These eddies then carry warm water shoreward across the shelf break. However, in coarse-resolution climate models, eddies are not resolved, resulting in the absence of warm water transport toward the shelf. To address this, we activate an additional scheme in the model that represents eddy fluxes at coarse resolution. This scheme can restore the missing transport and is most effective when it accounts for the slope of the ocean floor.

1 Introduction

The Cape Darnley region in East Antarctica (Fig. 1) is one of the major formation sites of Antarctic Bottom Water (AABW), with bottom water formed there contributing around 6–13% to the circumpolar volume of dense bottom water (Ohshima et al., 2013). Here, the formation of underwater frazil ice releases salt while keeping an insulating surface layer of sea ice from forming (Ohshima et al., 2022). Additionally, the opening of the polynya is facilitated by landfast ice and grounded icebergs that inhibit the advection of pack ice into the region (Ohshima et al., 2013; Fraser et al., 2019, 2020). Dense water is then advected along the continental slope (Wong & Riser, 2013; Aoki et al., 2020) and spreads into the Wild and Daly canyons (Nakayama et al., 2014; Mensah et al., 2021) while mixing with warmer modified Circumpolar Deep Water (mCDW, Hirano et al., 2015). Bottom water reaches the continental slope in April and displays short-term variability associated with baroclinic instability (Mizuta et al., 2021).

When dense water flows down the Antarctic continental slopes as gravity currents, the isopycnals bend downwards, linking the offshore CDW to the continental shelf (Thompson et al., 2018). Furthermore, gravity currents become baroclinically unstable during their descent and produce mesoscale eddies (Nakayama et al., 2014; Mack et al., 2019; A. L. Stew-

art, 2021). These eddies flux momentum upwards into the overlying warm Circumpolar Deep Water (CDW) and mechanically force it across the continental slope and onto the shelf (A. Stewart & Thompson, 2015, 2016; Morrison et al., 2020). The associated heat flux onto the shelf melts the base of Antarctic ice shelves, reduces their buttressing effect on the ice sheet, and ultimately accelerates the mass loss of the Antarctic Ice Sheet (Jacobs et al., 1992; Pritchard et al., 2012; Gudmundsson et al., 2019; Shepherd et al., 2018).

In an ocean model, a realistic representation of the down-slope flow of dense water and the onshore flow of CDW is only possible at eddy-resolving resolution (St-Laurent et al., 2013; A. Stewart & Thompson, 2015; Nakayama et al., 2014; Mensah et al., 2021). The first baroclinic Rossby radius of deformation on Antarctic continental shelves, however, is on the order of 5 km (Hallberg, 2013) and is still not resolved in state-of-the-art climate models. Thus, eddy-driven exchanges across the Antarctic continental slope need to be parameterized.

Mesoscale eddies are most commonly parameterized using the Gent and McWilliams/Redi schemes (GM/Redi, Redi, 1982; P. R. Gent & McWilliams, 1990; P. Gent et al., 1995). The GM scheme represents the advective effect of eddies through an additional advective tracer flux, and the Redi scheme produces tracer diffusion along isopycnals. Both schemes require setting a transfer coefficient, the GM and Redi diffusivities κ_{GM} and κ_{Redi}. Several schemes produce spatially varying transfer coefficients based on a mixing length approach (Green, 1970; Stone, 1972), in which the diffusivity is related to the product of an eddy velocity scale and a characteristic mixing length (Visbeck et al., 1997; Fox-Kemper & Ferrari, 2008; Cessi, 2008; Eden & Greatbatch, 2008; Jansen et al., 2015). More complex schemes integrate budget equations for the subgrid eddy energy, from which the transfer coefficients are derived (e.g., Eden & Greatbatch, 2008; Mak et al., 2018; Jansen et al., 2019).

The influence of sloping bottom topography is a major driver of spatial heterogeneity of eddy-driven tracer transports. Here, the topographic potential vorticity gradient effectively acts to suppress eddy fluxes (Sterl et al., 2024). In classical models of baroclinic instability (Eady, 1949; Phillips, 1954), the addition of a bottom slope produces a shift towards lower growth rates and length scales of unstable waves (Blumsack & Gierasch, 1972; Mechoso, 1980). Topographic suppression of eddies is also found in numerical ocean simulations (e.g., Isachsen, 2011; K. Brink, 2012; K. H. Brink & Cherian, 2013; A. L. Stewart & Thompson, 2013; Cimoli et al., 2017; K. H. Brink, 2016; Manucharyan & Isachsen, 2019; Chen et al., 2020), where the response to the bottom slope is more complex than the prediction of the linear Eady or Phillips model.

The suppressive effect of topography can be integrated into eddy parameterizations by adding a suppression function that locally reduces the transfer coefficients and, therefore, makes the parameterization "topography-aware". Such suppression functions can be constructed from diagnostic scalings based on, for example, the ratio of topographic and isopycnal slopes or the slope Burger number that can be derived from eddy-resolving idealized models (Wang & Stewart, 2020; Wei et al., 2022). Implemented into coarse-resolution channel models, a topography-aware GM scheme reduces the bias in the cross-slope tracer exchange, mean hydrographic fields, and slope current strength compared to the traditional version (Wei et al., 2024; Dettling et al., 2024). In an idealized model with dense water export over a continental slope, the modified parameterization improves cross-slope heat fluxes and moves CDW onshore (Dettling et al., 2024). Nummelin and Isachsen (2024) introduce a topography-aware GM/Redi scheme into a global model and thereby improve the representation of high-latitude density fronts locked to continental slopes that are otherwise strongly eroded by the GM/Redi scheme.

Based on an observationally validated regional model configuration of the Cape Darnley region (Mensah et al., 2021), we complement previous idealized modelling work (Dettling

et al., 2024) and investigate the influence of the GM/Redi parameterization on cross-slope transport in a setting with realistic topography and forcing. The small domain allows computationally affordable eddy-resolving reference simulations and ample numerical testing. We address the following questions:

1. What is the resolution dependence of eddy-driven onshore mCDW transports in the Cape Darnley region?
2. To what extent does the GM/Redi parameterization for mesoscale eddies improve the simulation of onshore mCDW transports?
3. How should the transfer coefficients of the GM/Redi parameterization be chosen?

2 Methods

2.1 Model configuration

In this study, we use a regional hydrostatic setup of the Massachusetts Institute of Technology general circulation model (MITgcm, J. Marshall et al., 1997; MITgcm Group, 2025) that has been extensively validated against observational records (Nakayama et al., 2014; Mensah et al., 2021). The numerical simulation accurately represents sea ice production, water mass distribution, and dense water export through the bathymetric canyons at eddy-resolving resolution (Nakayama et al., 2014; Mensah et al., 2021).

The setup includes thermodynamic and dynamic sea ice (Losch et al., 2010) and a landfast ice representation (Fraser et al., 2019, 2020). The topography is constructed from the General Bathymetric Chart of the Oceans (GEBCO) and the Australian Antarctic Division (AAD) 0.005° dataset, with additional refinements in the Wild Canyon (Mensah et al., 2021). At the surface, the model is forced by 6-hourly ERA-interim atmospheric reanalysis fields from the European Centre for Medium-Range Weather Forecast (ECMWF). At the lateral boundaries, the model is forced by monthly mean ocean velocities and sea ice conditions from the year 2008 of the ECCO LLC270 state estimate (Zhang et al., 2018) and seasonal temperature and salinity fields constructed from CTD measurements (Shimada et al., 2017). The vertical resolution increases from 10 m at the surface to 40 m at mid-depth, enough to satisfy the critical resolution necessary to resolve dense water gravity currents (Winton et al., 1998; Mensah et al., 2021). Additionally, partially filled cells are used to improve the representation of topography (Adcroft et al., 1997). We choose a 7th-order advection scheme and a non-linear equation of state (McDougall et al., 2003). Vertical diffusivity and viscosity are set to 5.5×10^{-6} m^2 s^{-1} and 1×10^{-4} m^2 s^{-1} in addition to setting a biharmonic horizontal viscosity (Leith, 1996). Momentum is extracted at the bottom using a quadratic bottom drag formulation with a drag coefficient of $c_d = 2.1 \times 10^{-3}$.

A simulation with a horizontal resolution of 2 km serves as our reference simulation. Here, the first baroclinic Rossby radius of deformation is resolved (Hallberg, 2013), and further increases in resolution do not produce major changes in the dense water export (Mensah et al., 2021). We then compare the results to coarse-grained versions of the configuration with resolutions of 8 km and 16 km. A resolution of 16 km ($\approx 1/3$ °S at 66 °S) represents the upper end of resolutions employed by state-of-the-art climate models and state estimate products (e.g., Haarsma et al., 2016; Zhang et al., 2018). The spinup procedure is the same as in Mensah et al. (2021). The model is spun up from climatological temperature and salinity profiles for one year at an intermediate resolution of 4 km. Subsequently, the model is run for two more years at resolutions of 2 km, 8 km, and 16 km. We then use the daily averaged model output of the second year for analysis. Using the first year instead does not result in significant differences.

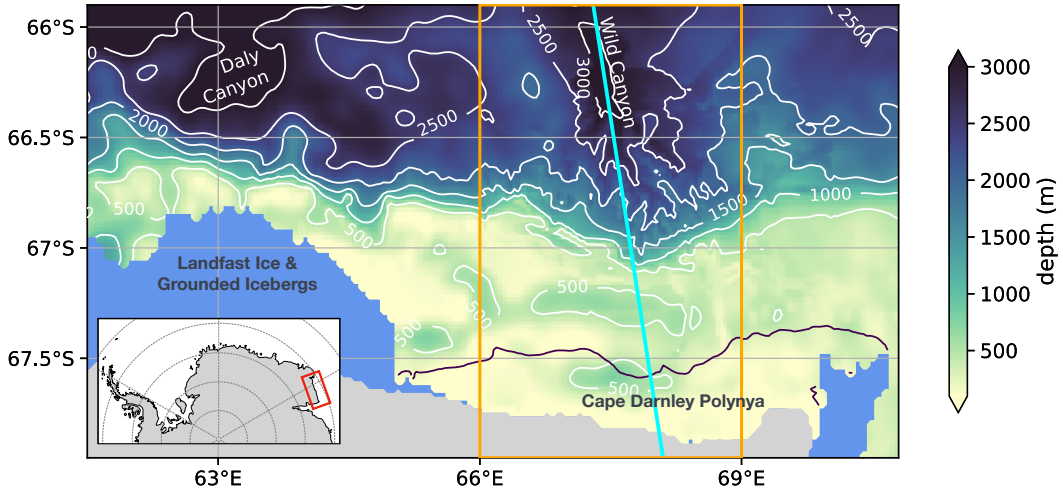

Figure 1. Bathymetry of the Cape Darnley regional model domain. The red box in the inset indicates the location of the Cape Darnley region. The blue area shows the landfast ice mask. The cyan line shows the Wild Canyon section along which model fields are plotted in Section 3. In Section 3, biases are computed in the area marked by the orange box (66–69 °E, 65.9–68 °S). In this box, the bathymetry is updated using surveys by R/V *Hakuho-maru* and *Shirase* (Mensah et al., 2021). The dark contour marks the Cape Darnley Polynya area where the simulated surface salt flux into the ocean exceeds 10^{-3} kg m^{-2} s^{-1} in the month of June.

We compute the eddy kinetic energy (EKE) as:

$$EKE = \frac{1}{2}\left(\overline{u'^2} + \overline{v'^2}\right), \tag{1}$$

where the overbar denotes a time average over the simulation period and the primes represent deviations from the time average. We also quantify the conversion rate from potential to eddy kinetic energy $PE \rightarrow EKE$:

$$PE \rightarrow EKE = g\left(\alpha\,\overline{w'\theta'} - \beta\,\overline{w'S'}\right), \tag{2}$$

with the gravitational acceleration g, thermal expansion and haline contraction coefficients α and β, potential temperature θ, salinity S, vertical velocity w. We further compute the vertical EKE flux $F_{z,\mathrm{EKE}}$:

$$F_{z,\mathrm{EKE}} = \overline{w'\phi'}, \tag{3}$$

where $\phi = p/\rho_0$, p is the dynamic pressure and ρ_0 is the reference density. Finally, the root mean square difference (RMSD) between a coarse-resolution model variable $\overline{\phi}_c$ and the corresponding coarse-grained high-resolution field $\overline{\phi}_{cg}$ is computed as:

$$RMSD = \sqrt{\sum_{x,\,y}\left(\overline{\phi}_c - \overline{\phi}_{cg}\right)^2}. \tag{4}$$

2.2 Gent and McWilliams/Redi parameterization for mesoscale eddies

To investigate the effect of an eddy parameterization, we repeat the coarse-resolution simulations and turn on the GM/Redi scheme. For an arbitrary tracer τ, the GM scheme

adds an advective flux divergence term to the right-hand side of the tracer equations:

$$F_{\mathrm{GM}} = -\nabla \cdot (\tau \mathbf{u}^*). \tag{5}$$

Here, the bolus velocity $\mathbf{u}^*$ is related to the isopycnal slopes, computed from the potential density σ as $s_{\mathrm{iso},x} = (\frac{\partial \sigma}{\partial x})/(-\frac{\partial \sigma}{\partial z})$ and $s_{\mathrm{iso},y} = (\frac{\partial \sigma}{\partial y})/(-\frac{\partial \sigma}{\partial z})$, following:

$$\mathbf{u}^* = \begin{pmatrix} -\partial_z(\kappa_{\mathrm{GM}} s_{\mathrm{iso},x}) \\ \partial_z(\kappa_{\mathrm{GM}} s_{\mathrm{iso},y}) \\ \partial_x(\kappa_{\mathrm{GM}} s_{\mathrm{iso},x}) + \partial_y(\kappa_{\mathrm{GM}} s_{\mathrm{iso},y}) \end{pmatrix}. \tag{6}$$

Additionally, the Redi scheme introduces a divergence term of isopycnal diffusion,

$$F_{\mathrm{Redi}} = \nabla \cdot (\kappa_{\mathrm{Redi}} \mathbf{K}_{\mathrm{Redi}} \nabla \tau), \tag{7}$$

where $\mathbf{K}_{\mathrm{Redi}}$ is the Redi tensor that rotates the tracer gradient to align with isopycnal surfaces. For simplicity, we set the GM and Redi coefficients κ_{GM} and κ_{Redi} to the same, vertically uniform, value $\kappa_{\mathrm{GM,Redi}}$. It is clear, however, that the GM and Redi schemes parameterize different physical processes and that eddy mixing varies in the vertical, both of which should eventually be reflected in the GM and Redi coefficients (e.g., Abernathey et al., 2013; Bachman et al., 2015).

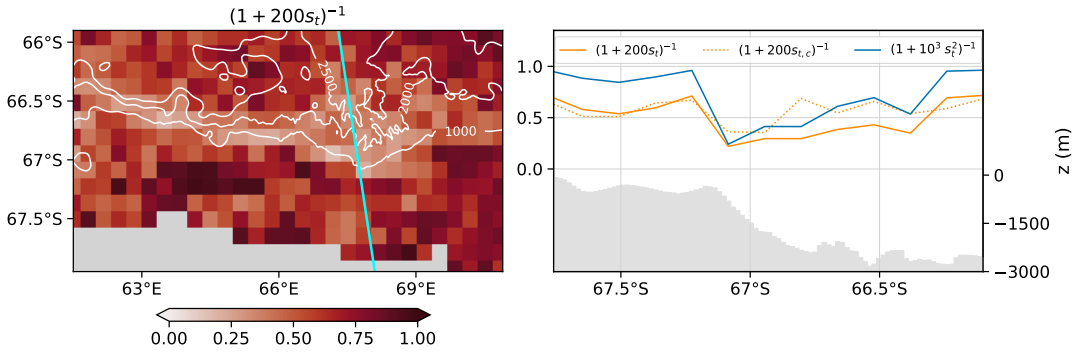

Figure 2. Linear topographic suppression factor following Eq. 9 in the model domain (a) and linear and quadratic (Eq. 9,10) suppression factors along the Wild Canyon section (b) at 16–km resolution. The stippled line shows the suppression factor computed from the slope of the 16–km resolution topography $s_{t,c}$. White contours and grey filling in panel (b) show the model topography at 2–km resolution.

Apart from setting a constant $\kappa_{\mathrm{GM,Redi}}$, we use a suppression function to make the eddy parameterization "topography-aware" (Fig. 2). Here, we adapt an empirical scaling of the form:

$$\kappa^{\mathrm{tl}}_{\mathrm{GM,Redi}} = \kappa_0 \, \frac{1}{1 + e \, B_s}, \tag{8}$$

where κ_0 is a constant reference GM/Redi diffusivity, $B_s = \overline{N}^z \, |s_t| \, / f_0$ is the slope Burger number, $\overline{N}^z$ is the vertically averaged buoyancy frequency, f_0 is the Coriolis parameter, s_t is the topographic slope and e is a tuning parameter (K. Brink, 2012; K. H. Brink & Cherian, 2013; K. H. Brink, 2016; Wei et al., 2022). Since s_t dominates the spatial variability of B_s in our setting, we simplify:

$$\kappa^{\mathrm{tl}}_{\mathrm{GM,Redi}} = \kappa_0 \, \frac{1}{1 + e_l \, s_t}. \tag{9}$$

For comparison, we also produce a topographic scaling based on the square of the topographic slope:

$$\kappa^{\mathrm{tq}}_{\mathrm{GM,Redi}} = \kappa_0 \, \frac{1}{1 + e_q \, s_t^2}. \tag{10}$$

Here, e_q was chosen so that the strongest supression over the continental slope matches the one produced by the linear form (Fig. 2,b).

For all simulations, $s_t = \sqrt{s_{t,\,x}^2 + s_{t,\,y}^2}$ is computed from the topography at 2-km horizontal resolution and interpolated to the coarse model grid. This is a simple and inexpensive way to pass subgrid information to the coarse-resolution simulation. Computing s_t from the coarse-resolution topography yields a more uniform suppression factor (Fig. 2,b) that performed slightly worse (not shown). Setting $e_l = 200$ and $e_q = 1 \times 10^4$ produces a suppression of the GM and Redi coefficients similar to previous studies (K. Brink, 2012; K. H. Brink & Cherian, 2013; K. H. Brink, 2016; Wei & Wang, 2021; Dettling et al., 2024). Choosing twice or half the values for e_l and e_q produced qualitatively similar results.

3 Results

3.1 Shoreward mCDW transport at eddy-resolving resolution

During austral autumn, there is a clear separation between the cold shelf waters and the mCDW further offshore (Fig. 3a). The isopycnals are nearly horizontal and for the mCDW layer they intersect the slope below the shelf break (Fig. 3c). Therefore, mCDW cannot directly access the shelf along an isopycnal. In winter, the dense water descent causes the isopycnals to bend downward, establishing an isopycnal connection between the mCDW layer on the slope and the continental shelf (Fig. 3d). The core of the mCDW shifts further south, and warm water — a mixture of mCDW, surface, and shelf waters — propagates across the shelf break near 67°S. This warm water is transported shoreward through the Wild and Daly Canyons and subsequently advected westward along the 1000-m isobath (Fig. 3b).

The EKE is generally low over most of the continental slope since eddies are suppressed by the steeply sloping topography (Fig. 4c). In winter, however, the EKE increases by several orders of magnitude compared to autumn values (Fig. 4d), especially on the upper continental slope. Hotspots of EKE are located shoreward of the topographic canyons, where eddies are generated during the baroclinically unstable downflow of dense water and convert PE to KE (Fig. 4b). Here, EKE is elevated throughout the whole water column (Fig. 4d), and there is an upward EKE flux into the mCDW layer, consistent with results from idealized model simulations (A. Stewart & Thompson, 2016).

The volume transport of the different water masses across the 1000-m isobath can be clearly distinguished when the transports are sorted by temperature (Fig. 5a). We chose the 1000-m isobath since the mCDW layer is located offshore of this depth in autumn, but the results do not depend on the choice of isobaths (not shown). Cold Antarctic Surface Water (AASW) and warm mCDW are transported shoreward across the 1000-m isobath, while at intermediate temperatures AABW flows offshore in the opposite direction. In the following, we use the transport extrema in Fig. 5a to distinguish these water masses (-1.64 °C and -0.39 °C). At high frequency, mCDW and AABW transports are correlated in time (correlation coefficient of $r = 0.81$), consistent with their eddying nature.

A comprehensive observational validation of these results is challenging due to sparse measurements on the shelf, especially in winter, and due to the eddying nature of the on-shelf transports. Generally, the simulated hydrographic conditions compare favorably to datasets reconstructed from historical CTD, Argo and biologging data and the sea ice production in the polynya region agrees well with satellite observations (Mensah et

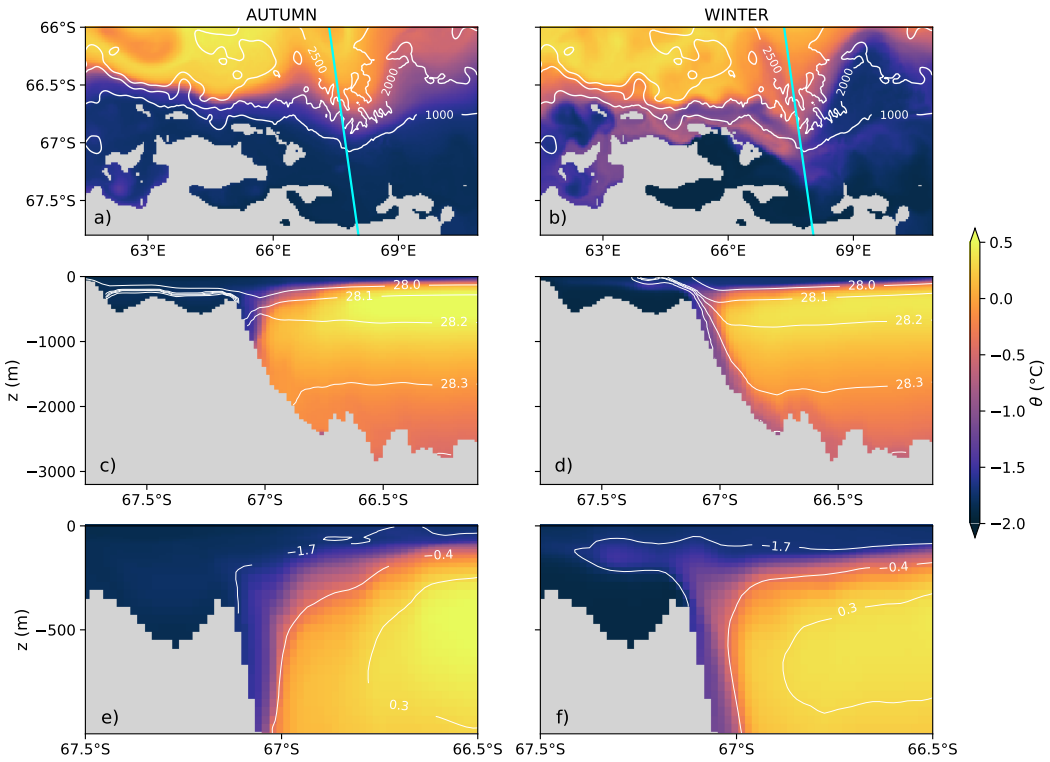

Figure 3. 170–m potential temperature (color shading) and bathymetry (white contours) for February–May (a) and June–September (b). The cyan line indicates the Wild Canyon section plotted in panels c-f, and the yellow arrows illustrate the pathway of warm water across the slope. Wild Canyon section of potential temperature (color shading) and neutral density (white contours) for the same periods (c,d). Close-up of potential temperature (color shading and white contours) for the same periods (e,f).

al., 2021, their figures 3 and 4). Additionally, the T-S-properties and velocities of the simulated dense water downflow closely resemble those recorded by moorings in Wild Canyon (Mensah et al., 2021, their figures 10–12). In 2010, mooring records on the upper slope of Wild Canyon show periods of elevated temperatures of up to -1 °C in August and September. CTD casts in the same time period indicate that this water is a mixture of mCDW and DSW (Ohshima et al., 2022, their figure 2). Hydrographic data along a section through Wild Canyon further show a very similar temperature and density structure to Fig. 3d with isopycnals bending upward to connect warm mCDW to the shelf (Mizuta et al., 2024, their figure 6).

3.2 Resolution dependence of cross-slope transports

Changing the grid spacing to 8 and 16 km significantly affects the onshore mCDW and offshore AABW transports (Fig. 6). At 16-km resolution, the downslope AABW transport decreases by 22.6%, while the upslope mCDW transport is reduced by 64.8% compared to the 2-km reference simulation. At 8 km, the differences relative to the high-resolution case are smaller, and the AABW transport even shows a slight increase. The first baroclinic Rossby radius ranges from 6 km on the upper slope to 8 km on the lower slope, suggesting that at 8-km resolution, eddies responsible for the cross-slope warm-water transport are still partially resolved. However, the EKE is orders of magnitude lower than in

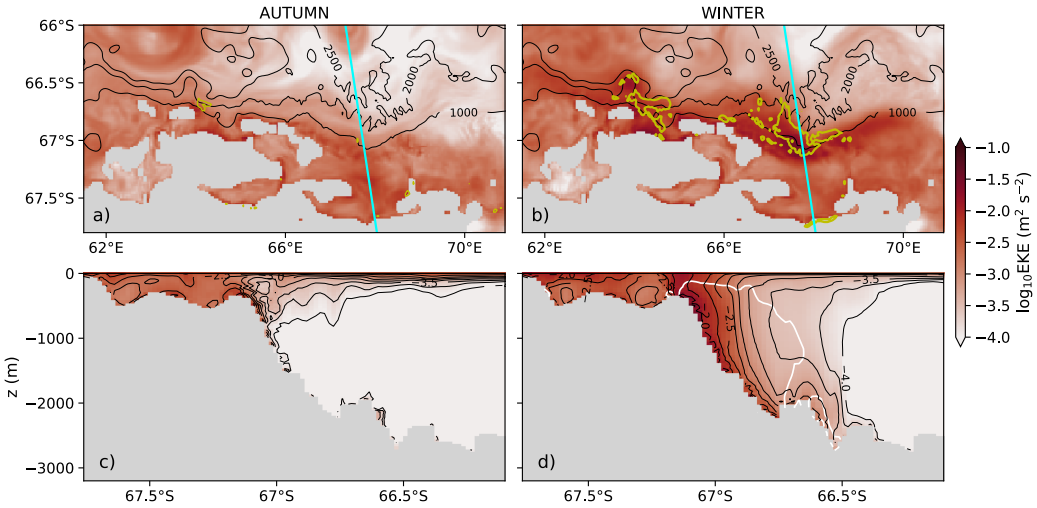

Figure 4. Vertically integrated EKE (color shading), bathymetry (black contours), and PE to EKE conversion rate (blue contour, shown is the 5×10^{-6} m^3 s^{-3} contour line) for February–May (a) and June–September (b). Wild Canyon section of EKE (color shading and black contours) for the same periods (c,d). The white contour encloses areas where the upward EKE flux exceeds 5×10^{-7} m^3 s^{-3}.

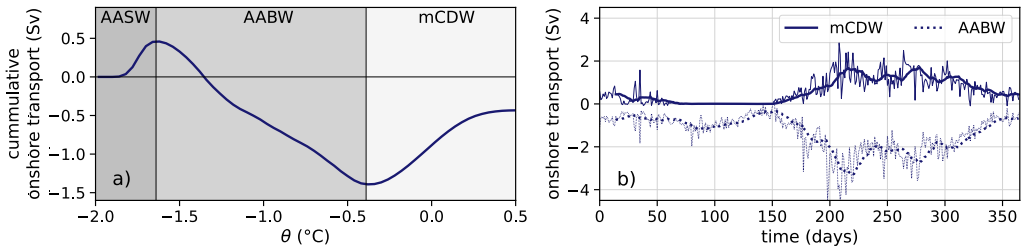

Figure 5. Onshore volume transports across the 1000-m isobath, cumulatively integrated from low to high temperature (a) and time evolution of contributions from mCDW and AABW (b). Thick lines represent a 15-day running average in time; thin lines are constructed from daily averages (b).

the 2-km run (Fig. S1), and farther downslope, the dense water signal is lost due to excessive numerical diffusion (Mensah et al., 2021). We therefore focus our parameterization work on the 16-km simulations.

When a coarser resolution is used, the vertical extent and the temperature of the gravity current strongly increase (Fig. 7). This is a well-documented phenomenon in z-coordinate ocean models, where the step-wise representation of topography leads to excessive vertical mixing and entrainment of overlying waters (Winton et al., 1998; Legg et al., 2009). Considering an average plume thickness of $H = 350$ m and a topographic slope of $\alpha = 0.068$, an estimate of the critical horizontal resolution yields $\Delta x_c = H/2\alpha \approx 2$ km (Mensah et al., 2021).

At horizontal resolutions of 8 and 16 km, the mCDW core is slightly colder compared to the reference run and does not extend as far south. The isopycnals delineat-

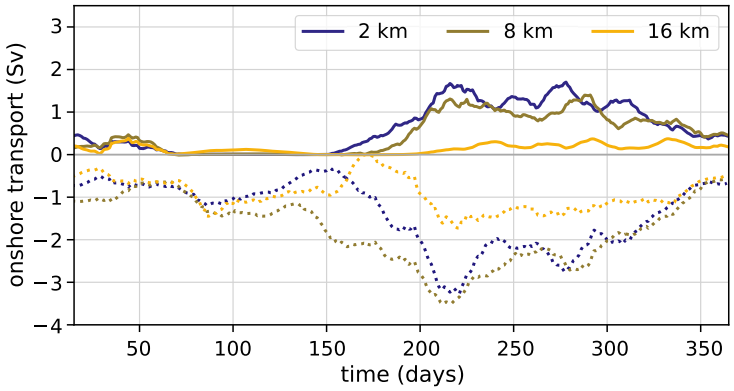

Figure 6. 15–day running average of onshore volume transports across the 1000-m isobath, separated into mCDW (solid) and AABW (dashed) for horizontal resolutions of 2 km, 8 km, and 16 km.

ing the mCDW layer converge at the shelf break and act as a barrier for onshore mCDW transport. This results in lower temperatures on the shelf compared to the reference (see also Fig. 9 for a close-up on the shelf break).

3.3 Parameterizing cross-slope mCDW transports

After establishing the effect of horizontal resolution, we now turn to parameterizing the eddy-driven transport of mCDW using the GM/Redi scheme. To this end, we focus on the 16-km resolution model setup, where the differences to the reference simulation are large. We concentrate our analysis on the Wild Canyon section, where eddy-driven processes dominate at high resolution.

The GM/Redi parameterization generally improves the simulated temperature at sites of dense water export (Fig. 7,8,g,i). With the eddy parameterization switched on, the model recovers a core of mCDW over the lower continental slope and simulates a transport of warm water across the shelf break (Fig. 9). With the topography-aware GM/Redi scheme, the -1.7 °C–isotherm reaches approximately the same latitude as in the high-resolution reference simulation (Fig. 9d). When the traditional scheme is used, the warm water transport across the shelf break reaches too far onto the shelf and is generally too warm (Fig. 9c). In both cases, the warm water intrusion occurs at larger depths than in the reference run. We attribute this bias to the coarse-grained topography that does not resolve important details (Figs. 7,9) and a tapering of the GM/Redi near the surface, which we will discuss in section 3.4 below. Indeed, the temperature maxium lies at greater depth when running the model at high-resolution and with a coarse-grained tropography (not shown).

Salinity also improves locally (Fig. 7,8, right column). Here, the lateral exchange of shelf water produced by the GM/Redi scheme homogenizes the salinity on the shelf and reduces the anomalous accumulation of salt seen in the runs without the eddy parameterization.

More generally, the GM/Redi scheme reduces the RMSD of vertically averaged temperature between the simulations employing high and coarse resolutions (Fig. 10). With constant GM/Redi coefficients, the biggest overall improvement is achieved with coefficients of around 600 $m^2\ s^{-1}$. In contrast, the vertical maximum of temperature, mark-

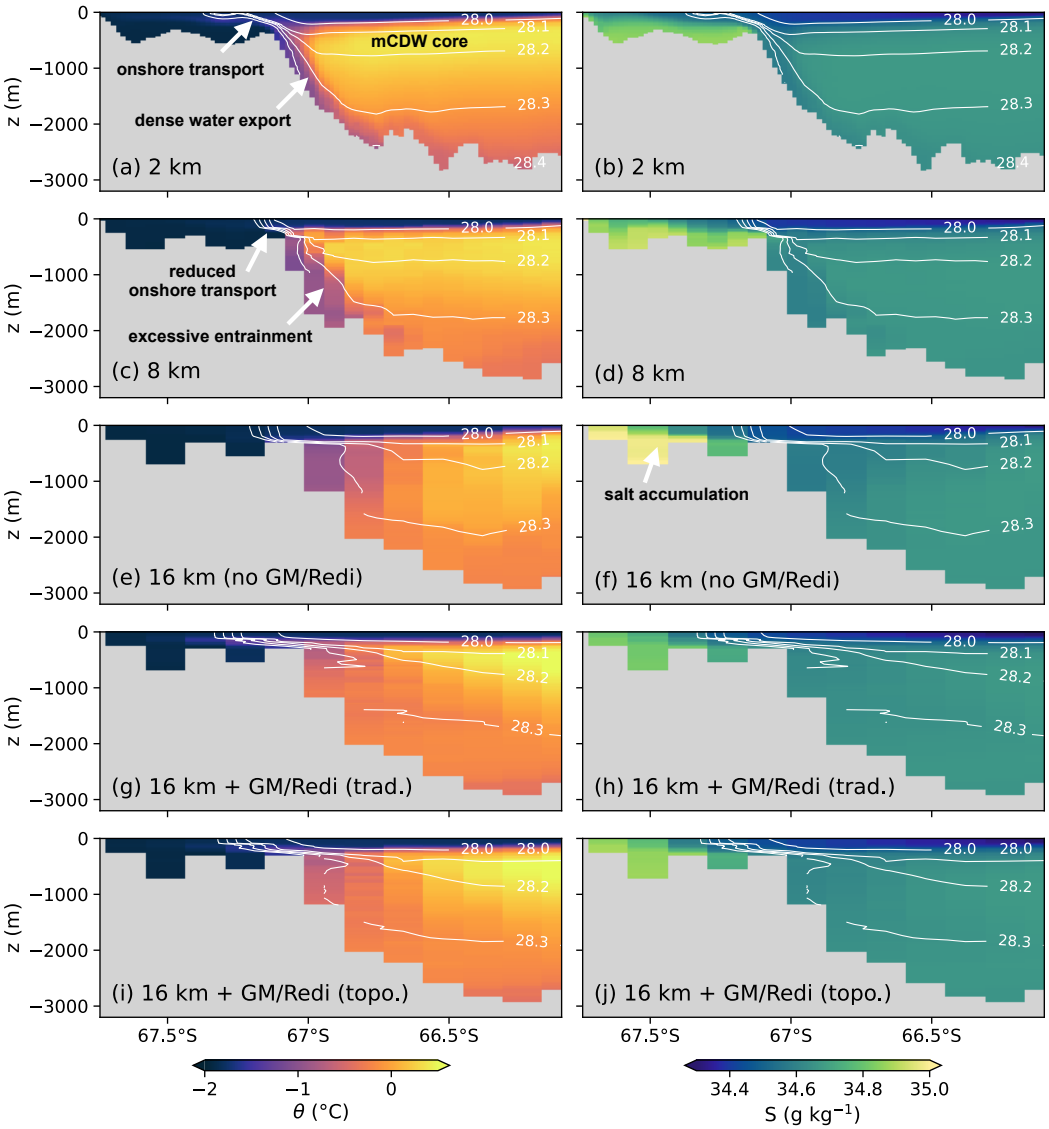

Figure 7. Wild Canyon section of potential temperature and salinity averaged over June–September at horizontal resolutions of 2 km (a-b), 8 km (c,d) and 16 km without GM/Redi (e,f). Panels (g-j) show potential temperature and salinity at 16-km resolution using the traditional ($\kappa_{\mathrm{GM,Redi}} = 600$ m^2 s^{-1}) and topography-aware GM/Redi scheme (Eq. 9) where the domain-averaged $\kappa_{\mathrm{GM,Redi}} \approx 600$ m^2 s^{-1}. Contours show neutral density.

ing the mCDW layer, is best represented at lower GM/Redi coefficients of 300 m^2 s^{-1}. With higher coefficients, the error in the mCDW temperature increases again whereas the temperature in the rest of the domain continues to improve. We conclude that simulations with high coefficients, which produce the smallest error in most of the domain, overestimate the transport of mCDW across the shelf break.

In addition to the temperature sections (Fig. 9), vertical profiles and time series of temperature at the shelf break and inner shelf of Wild Canyon also indicate an overly strong warm water transport at high constant GM coefficients (Fig. 11). This is similar to the results of an idealized model, where high coefficients fitting the shelf and open

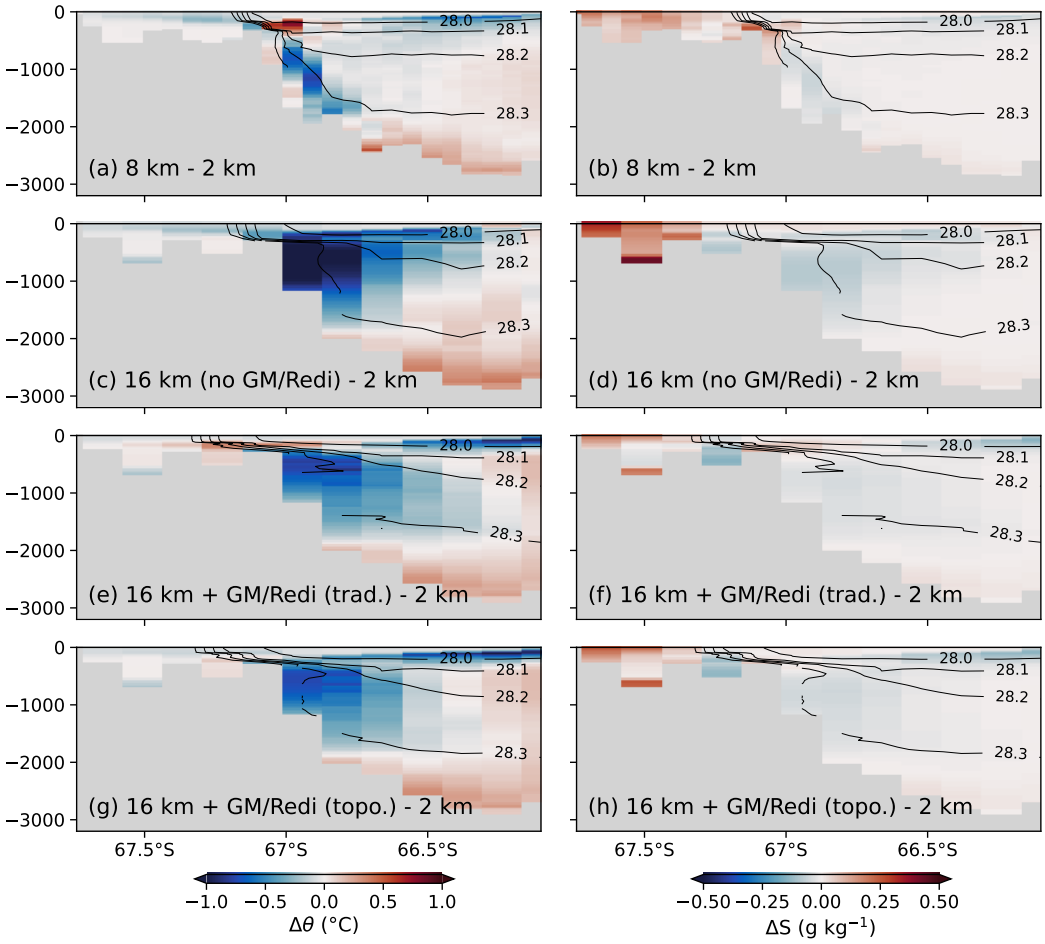

Figure 8. Same as Fig. 7, but for the difference between the sensitivity runs and the coarse-grained 2-km resolution simulation.

ocean section are too large over the continental slope and lead to an overestimation of the transport of mCDW across the shelf break (Dettling et al., 2024).

The topography-aware GM scheme reduces the GM/Redi coefficients where the topographic slope limits eddy-driven exchange at high resolution and, at the same time, retains large coefficients over flat-bottom areas. As a result, the temperature errors on the shelf continue to reduce with higher background coefficients (Fig. 10). In particular, the representation of the maximum temperature, that is, the mCDW temperature, improves with reduced GM coefficient over steep slopes. The advantage of the modified GM/Redi parameterization also emerges in the time series and vertical profiles of temperature, where the topography-aware version reproduces the reference temperature much better compared to the run with the traditional eddy parameterization (Fig. 11). Admittedly, the performance of the traditional GM/Redi scheme at this particular location could have been improved by selecting a smaller constant GM/Redi diffusivity. This, however, comes at the expense of larger errors elsewhere in the domain (see also Dettling et al., 2024). In summary, when choosing constant GM/Redi diffusivities, one has to choose between the best representation of the mCDW transport across the slope and the strongest improvement in the temperature field over the whole domain. The topography-aware GM/Redi scheme offers a compromise by simultaneously improving both aspects.

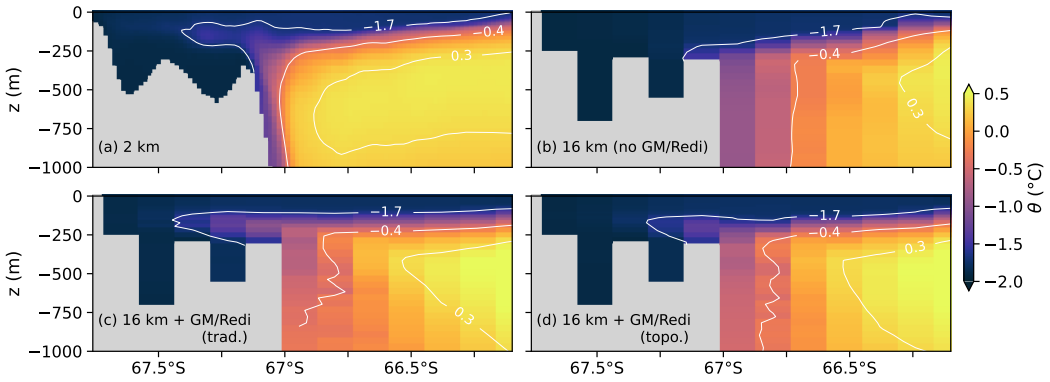

Figure 9. Shelf break of the Wild Canyon section. Color shading shows the potential temperature averaged over June–September at 2-km (a) and 16-km (b-d) horizontal resolution. Panel (b) shows the run without GM/Redi, panel (c) the run using the traditional GM/Redi scheme ($\kappa_{\mathrm{GM,Redi}} \approx 600\ \mathrm{m^2\ s^{-1}}$), and panel (d) the one using the topography-aware GM/Redi scheme (Eq. 9) where the domain-averaged $\kappa_{\mathrm{GM,Redi}} \approx 600\ \mathrm{m^2\ s^{-1}}$. Contours show potential temperature.

Salinity improves linearly with higher GM coefficients (Fig. 12). Here, the salinity error is mainly determined by the shelf section, where the GM/Redi parameterization helps to distribute the salt input by sea ice formation laterally (Fig. 7,f,j). Arguably, the salinity error does not represent a suitable tuning metric here since the improvement is mainly limited to a few grid cells at the edge of the domain. Since the salinity error on the shelf is local and only weakly affected by cross-slope exchange, the use of the topography-aware GM/Redi scheme only produces minor changes compared to the traditional version.

The linear and quadratic forms of the topographic suppression factor produce only slightly different results (Figs. 10, 12). As we tune it here, the linear form leads to a stronger overall reduction of the GM/Redi coefficients—even with moderate topographic slopes (Fig. 2,b)—whereas the quadratic form results in a more localized suppression. Consequently, the quadratic form is more similar to the case with constant $\kappa_{\mathrm{GM,Redi}}$ and reduces the RMSDs of vertically averaged hydrographic fields slightly less than the linear form.

The linear form, however, seems to be the better choice when aiming to improve the maximum temperature. We note that both scalings are empirical and, therefore, bear little physical justification. Scalings derived from dynamical considerations (e.g., Sterl et al., 2024) may perform better than the ones presented here but are much more difficult to implement and still require tuning.

A combination of the GM and the Redi scheme is needed to improve the representation of cross-slope warm water transport (Fig. 13). If only the GM scheme is used, warm water is transported across the continental slope, but there is too little transport across the shelf break. If only the Redi scheme is employed, the warm water remains further offshore, limiting the potential for on-shore diffusive heat fluxes. The domain-integrated RMSD errors are always higher compared to simulations using a combination of both schemes (not shown). This is consistent with idealized high-resolution model simulations where eddy advection dominates over the slope, whereas eddy diffusion is responsible for tracer exchange across the shelf break (A. Stewart & Thompson, 2016). Similarly, idealized simulations with the GM/Redi scheme show that the GM scheme dominates over

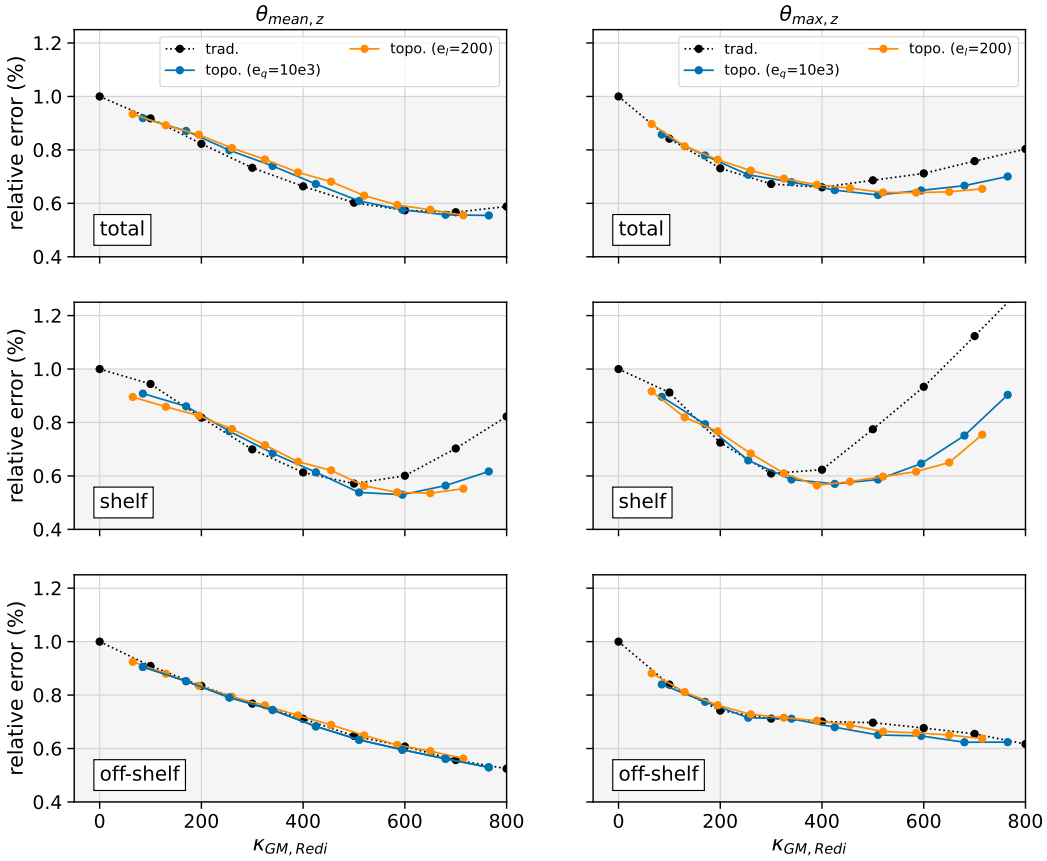

Figure 10. Root mean square differences (RMSDs) of vertically averaged potential temperature (left column) and the vertical temperature maximum (right column) for different values of the GM/Redi diffusivity in the Wild Canyon area (orange box in Fig. 1). RMSDs are computed with respect to the 2-km run and scaled by the RMSD of the run without an eddy parameterization. Values smaller than 1 (grey area) represent an improvement. The black dashed curves show RMSDs for simulations employing the traditional GM/Redi scheme with constant coefficients. The solid curves represent the simulations with the topography-aware GM/Redi scheme following Eq. 9 with $e_l = 200$ (yellow curve) and Eq. 10 with $e_q = 10^4$ (blue curve). Markers are plotted at their respective domain-averaged κ_{GM}.

the slope while the Redi scheme is more important over the shelf break (Dettling et al., 2024).

3.4 Influence of the GM tapering scheme

It is common practice to use a tapering scheme in conjunction with the GM/Redi scheme to avoid numerical instability. The tapering scheme reduces the influence of GM/Redi, where steep isopycnal slopes would otherwise trigger an overly strong response of the parameterization (Cox, 1987). In this study, we use a tapering scheme that produces smooth tapering as a function of the local isopycnal slope s_{iso} and two tuning parameters s_d and s_c (Danabasoglu & Williams, 1995):

$$f_1(S) = \frac{1}{2}\left[1 + \tanh\left(\frac{s_c - |s_{\mathrm{iso}}|}{s_d}\right)\right]. \tag{11}$$

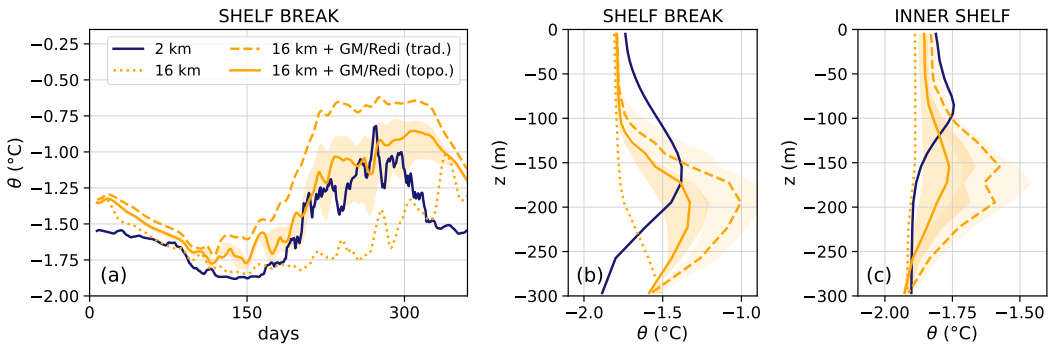

Figure 11. 200-m potential temperature timeseries (a) and depth profile averaged over June-September (b, c) at the Wild Canyon shelf break (67.1 °S) and inner continental shelf (67.4 °S). The orange lines represent coarse-resolution runs with no GM/Redi (dotted line), the GM/Redi parameterization in the traditional version (dashed line, $\kappa_{\mathrm{GM,Redi}} = 600\ \mathrm{m^2\ s^{-1}}$) and in the topography-aware version (solid line, Eq. 9) where the domain-averaged $\kappa_{\mathrm{GM,Redi}} \approx 600\ \mathrm{m^2\ s^{-1}}$. The shadings indicate the temperature range obtained by changing $\kappa_{\mathrm{GM,Redi}}$ by $\pm$ 200 $\mathrm{m^2\ s^{-1}}$.

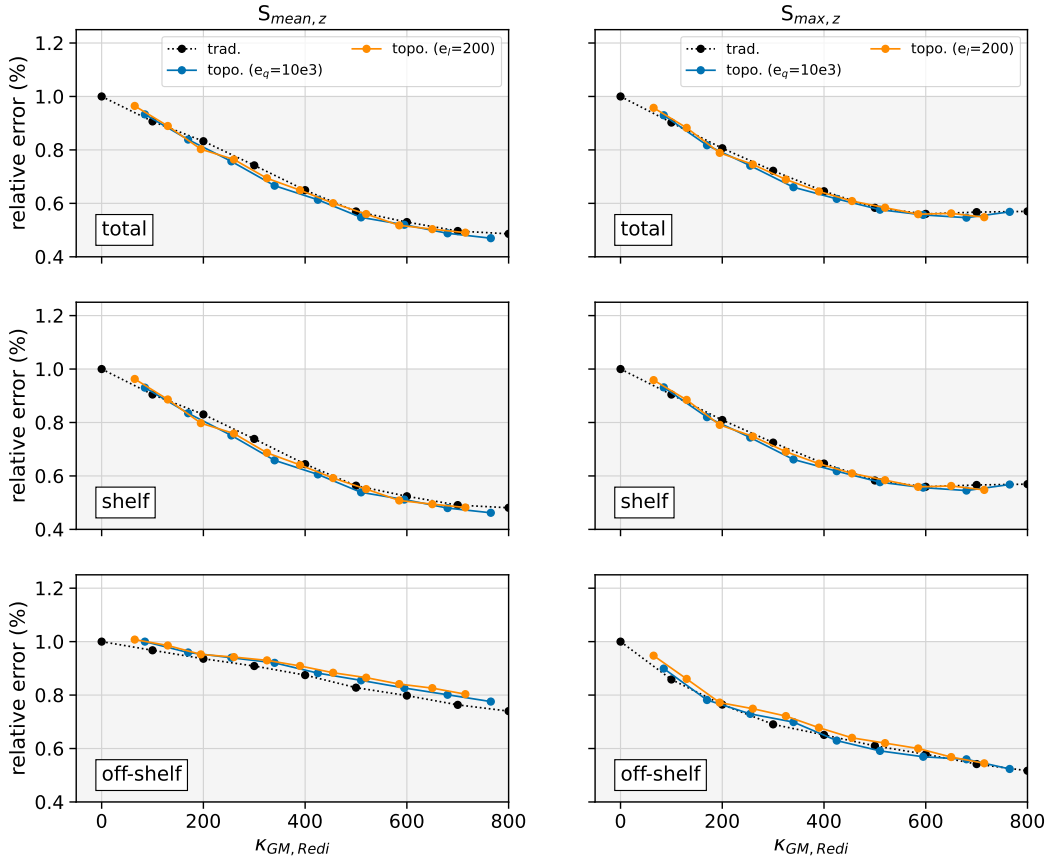

Figure 12. Same as Fig. 10 but for salinity.

Additionally, we employ a second tapering scheme that reduces the effect of GM/Redi close to the surface. This avoids conflicts between the vertical mixing scheme, which acts to steepen isopycnals in the presence of surface forcing, and the eddy parameterization

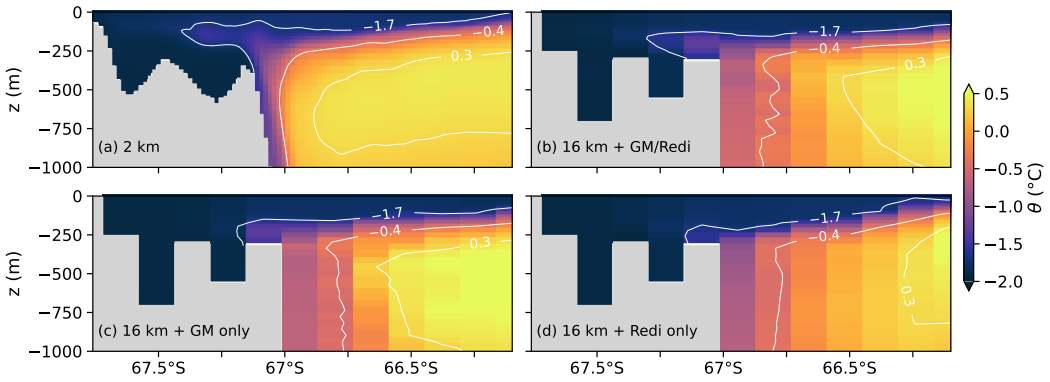

Figure 13. Shelf break of the Wild Canyon section. Color shading shows the potential temperature averaged over June–September at 2-km (a) and 16-km (b-d) horizontal resolution. Panel (b) shows the run using the topography-aware GM/Redi scheme (Eq. 9) where the domain-averaged $\kappa_{\mathrm{GM,Redi}} \approx 600\ \mathrm{m^2\ s^{-1}}$. The lower panels show simulations with only the topography-aware GM scheme (c) and only the topography-aware Redi scheme (d), using the same coefficients as in (b).

(Large et al., 1997):

$$f_2(S) = \frac{1}{2}\left[1 + \sin\left(\pi \frac{z}{D} - \frac{\pi}{2}\right)\right]. \tag{12}$$

Here, z is depth and $D = (c/f)|s_{\mathrm{iso}}|$ is the vertical displacement that a water parcel experiences while moving along an isopycnal over the distance of the Rossby Radius c/f, with Coriolis parameter f and the first baroclinic wave speed $c = 2\,\mathrm{m\,s^{-1}}$ (Large et al., 1997, their Appendix B). In all of our simulations, the GM/Redi contributions (Eq. 5, 7) are thus scaled by $f_1 \times f_2$.

During the dense water export period, the continental slope in the Cape Darnley region supports steep isopycnal slopes at greater depths (Fig. 3d). With the commonly used default values of $s_c = 0.004$ and $s_d = 0.001$, these slopes imply strong tapering (Fig. 14), and the GM/Redi coefficients are tapered to almost zero over most of the continental slope (Fig. 15a). Consequently, the model solution is essentially the same as when the parameterization is switched off completely and no cross-slope transport of warm water is simulated (Fig. S2). Therefore, we adjusted the values of $s_c = 0.2$ and $s_d = 0.05$ to match the steepest section of the continental slope in the model domain so that GM/Redi can act on steeper isopycnal slopes. With the adjusted settings, the tapering is reduced over the continental slope (Fig. 15b). In summary, the tapering scheme needs to be adjusted to effectively use GM/Redi over continental slopes and to benefit from the topography-aware GM scheme.

4 Summary and discussion

In an eddy-resolving regional model, the down-slope flow of dense water in the Cape Darnley region generates eddies that drive a shoreward transport of warm mCDW across the continental shelf break. This transport is strongly reduced when running the model at a coarse resolution typical for climate models. With the GM/Redi parameterization turned on, the model produces a warm water transport across the shelf break of Wild Canyon and simulates improved hydrographic mean fields. We find that small coefficients are needed to simulate a cross-slope warm water transport consistent with the reference simulation, whereas larger coefficients improve the hydrographic mean state on the shelf and in the open ocean section. Therefore, we employ a topography-aware version of the

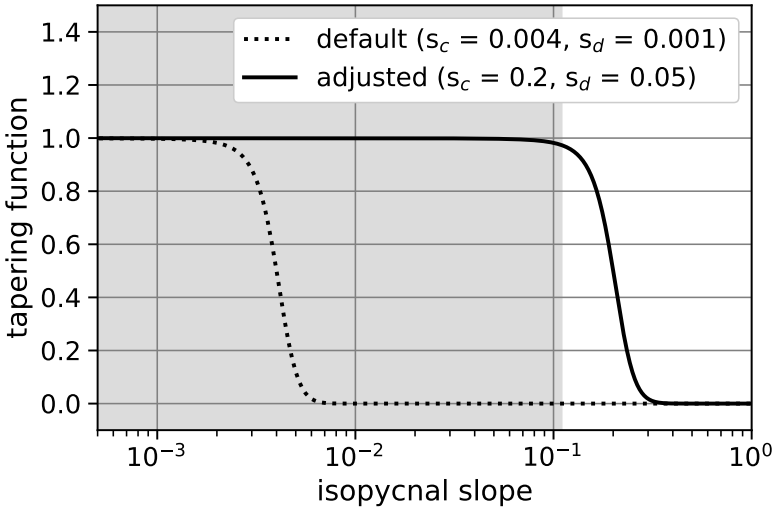

Figure 14. Tapering function f_1 (Danabasoglu & Williams, 1995) with default ($s_d = 0.001$, $s_c = 0.004$) and adjusted ($s_d = 0.05$, $s_c = 0.2$) tuning parameters. The grey area shows the range of topographic slopes present in the model domain.

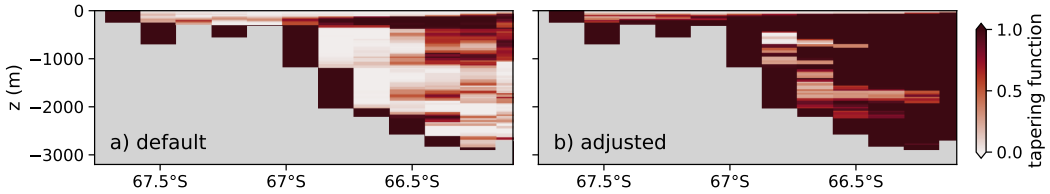

Figure 15. Tapering function $f_1 \times f_2$ (Danabasoglu & Williams, 1995; Large et al., 1997) at the Wild Canyon section for June–September with (a) default ($s_d = 0.001$, $s_c = 0.004$) and (b) adjusted ($s_d = 0.05$, $s_c = 0.2$) tuning parameters.

GM/Redi scheme, reducing the transfer coefficients over the continental slope where eddies are suppressed at high resolution. When using the spatially varying GM/Redi coefficients, the model produces the correct warm water transport across the shelf break and simultaneously improves the hydrographic fields on the shelf and offshore.

There are various ways to refine the topography-aware GM/Redi scheme further. We chose a very simplified topographic scaling that does not require an online computation of the topographic suppression function. The reason for this choice is to limit the number of tuning parameters and to offer an approach that is fast and easy to adopt. Some spatial and temporal variability could be introduced by retaining the buoyancy frequency in the Burger number-based scaling. Alternatively, there are analytically derived scaling functions that are dynamically more consistent but require additional parameterizations that we did not attempt here (Sterl et al., 2024; Nummelin & Isachsen, 2024). Secondly, there are more elaborate ways of generating spatially varying GM/Redi coefficients before applying the topographic suppression function. An example is the GEOMETRIC scheme (D. P. Marshall et al., 2012; Mak et al., 2018), where the tendency terms of eddy energy need to be parameterized. Finally, the GM/Redi scheme can suppress resolved eddies—an effect we also observe in our simulations, although only to a small extent. One potential solution is to filter the density field and apply GM/Redi only to the background isopycnal slope (Mak et al., 2023).

Our results suggest that the effective use of a topography-aware GM/Redi scheme over continental slopes requires modifications to the tapering scheme. At very coarse resolution, it may be desirable to taper GM/Redi close to the boundary. Simulations at intermediate resolutions where continental slopes are resolved, however, can be expected to benefit from an eddy parameterization if carefully applied. One could, for example, extend existing schemes (e.g., Gerdes et al., 1991; Large et al., 1997; Danabasoglu & Williams, 1995) so that they produce spatially varying tapering, allowing for isopycnals to slope as steeply as the local topographic slope.

The continental slope in the Cape Darnley region is steeper compared to other sites of dense water export, such as the Weddell Sea, and is rich in small-scale structure. Consequently, it is a particularly tough problem with respect to typical issues such as the poor representation of overflows. Motivated by the performance of topography-aware GM/Redi schemes in idealized simulations with moderate slopes (Wei et al., 2024; Dettling et al., 2024), we can speculate that a topography-aware GM/Redi scheme may perform even better when the bottom slope is more gentle and more uniform. This hypothesis remains to be tested in regional models of other sections of the Antarctic continental slope.

We run the regional model for one individual year for which it has been validated against observations (Nakayama et al., 2014; Mensah et al., 2021). The production and export of dense water from the Cape Darnley region displays interannual variability and has likely increased over the last 20 years (Gao et al., 2022). Whether a coarse model with our modifications to the GM/Redi scheme reproduces such variability remains to be tested. In an idealized model, an increase in dense water export drives stronger onshore heat fluxes (Si et al., 2023). These heat fluxes are not correctly captured by the traditional GM/Redi scheme, but a topography-aware version may offer a way forward.

Simulating realistic water mass properties on the continental shelves of Antarctica is essential for producing robust estimates of, for example, ice shelf melt and the associated sea level rise (van Westen & Dijkstra, 2021). As we show here, parameterizing the effects of mesoscale eddies at coarse resolution is imperative to achieve this goal. Ocean reanalysis products with an eddy parameterization are often interpreted as the best estimate of the ocean state but still fail to reproduce the observed hydrography and circulation on the Antarctic continental shelves (Nakayama et al., 2024). In particular, most of the simulated shelf temperatures show warm biases, pointing towards an overly strong cross-slope exchange of CDW. Here, we have successfully addressed the issue of too-strong cross-slope mCDW transports by modifying the GM/Redi coefficients and tapering scheme. It may therefore be worth testing this strategy in the model configurations that produce the current state-estimates. We anticipate that the improved performance of the topography-aware GM/Redi scheme compared to the traditional version also holds for other sections of the Antarctic continental slope. Thus, the integration of topography-aware eddy parameterizations may contribute to bringing the simulated hydrography on Antarctic continental shelves closer to observations. We therefore encourage the implementation and further testing of topography-aware eddy parameterizations in ocean models.

Open Research Section

The MITgcm code can be accessed https://github.com/MITgcm, and documentation is provided at https://mitgcm.readthedocs.io/en/latest. Namelists and input files for reproducing the high-resolution reference run can be found in Mensah (2021). Namelists and input files for reproducing the coarse-resolution runs can be found in Dettling (2025a), and model output is stored in Dettling (2025b).

Acknowledgments

This paper is a contribution to the project T3 (Energy Transfers in Gravity Currents) of the Collaborative Research Centre TRR 181 "Energy Transfers in Atmosphere and Ocean" funded by the Deutsche Forschungsgemeinschaft (DFG, German Research Foundation, project number 274762653). YN was supported by the funds from Grants-in-Aid for Scientific Research of the Japanese Ministry of Education, Culture, Sports, Science and Technology (24K15256,24H02341) and by a grant from NASA Sea Level Change Team (80NSSC24K1532). We thank the editor and three anonymous reviewers for their constructive comments.

References

Abernathey, R., Ferreira, D., & Klocker, A. (2013). Diagnostics of isopycnal mixing in a circumpolar channel. *Ocean Modelling*, *72*, 1-16. doi: 10.1016/j.ocemod.2013.07.004

Adcroft, A., Hill, C., & Marshall, J. (1997). Representation of topography by shaved cells in a height coordinate ocean model. *Monthly Weather Review*, *125*(9), 2293 - 2315. doi: 10.1175/1520-0493(1997)125⟨2293:ROTBSC⟩2.0.CO;2

Aoki, S., Katsumata, K., Hamaguchi, M., Noda, A., Kitade, Y., Shimada, K., ... others (2020). Freshening of Antarctic bottom water off Cape Darnley, East Antarctica. *Journal of Geophysical Research: Oceans*, *125*(8), e2020JC016374.

Bachman, S., Fox-Kemper, B., & Bryan, F. (2015). A tracer-based inversion method for diagnosing eddy-induced diffusivity and advection. *Ocean Modelling*, *86*, 1-14. doi: https://doi.org/10.1016/j.ocemod.2014.11.006

Blumsack, S. L., & Gierasch, P. J. (1972). Mars: The effects of topography on baroclinic instability. *Journal of Atmospheric Sciences*, *29*(6), 1081 - 1089. doi: 10.1175/1520-0469(1972)029⟨1081:MTEOTO⟩2.0.CO;2

Brink, K. (2012, 07). Baroclinic instability of an idealized tidal mixing front. *Journal of Marine Research*, *70*. doi: 10.1357/002224012805262716

Brink, K. H. (2016). Continental shelf baroclinic instability. Part I: Relaxation from upwelling or downwelling. *Journal of Physical Oceanography*, *46*(2), 551 - 568. doi: 10.1175/JPO-D-15-0047.1

Brink, K. H., & Cherian, D. A. (2013). Instability of an idealized tidal mixing front: Symmetric instabilities and frictional effects. *Journal of Marine Research*, *71*(6), 425-450. doi: doi:10.1357/002224013812587582

Cessi, P. (2008). An energy-constrained parameterization of eddy buoyancy flux. *Journal of Physical Oceanography*, *38*(8), 1807 - 1819. doi: 10.1175/2007JPO3812.1

Chen, S.-N., Chen, C.-J., & Lerczak, J. A. (2020). On baroclinic instability over continental shelves: Testing the utility of Eady-type models. *Journal of Physical Oceanography*, *50*(1), 3 - 33. doi: 10.1175/JPO-D-19-0175.1

Cimoli, L., Stegner, A., & Roullet, G. (2017). Meanders and eddy formation by a buoyant coastal current flowing over a sloping topography. *Ocean Science*, *13*(6), 905–923. Retrieved from `https://os.copernicus.org/articles/13/905/2017/` doi: 10.5194/os-13-905-2017

Cox, M. (1987). Isopycnal diffusion in a z-coordinate ocean model. *Ocean modelling*, *74*, 1–5.

Danabasoglu, G., & Williams, J. C. M. (1995). Sensitivity of the global ocean circulation to parameterizations of mesoscale tracer transports. *Journal of Climate*, *8*(12), 2967 - 2987. doi: 10.1175/1520-0442(1995)008⟨2967:SOTGOC⟩2.0.CO;2

Dettling, N. (2025a). *MITgcm configurations for "A topography-aware eddy parameterization improves warm water transport across the Cape Darnley continental slope" [configuration].* doi: https://doi.org/10.5281/zenodo.15090171

Dettling, N. (2025b). *MITgcm model output for "A topography-aware eddy parameterization improves warm water transport across the Cape Darnley continental slope" [data].* doi: https://doi.org/10.5281/zenodo.15095123

Dettling, N., Losch, M., Pollmann, F., & Kanzow, T. (2024, 06). Towards parameterizing eddy-mediated transport of Warm Deep Water across the Weddell Sea continental slope. *Journal of Physical Oceanography*. doi: 10.1175/JPO-D-23-0215.1

Eady, E. T. (1949). Long waves and cyclone waves. *Tellus*, *1*(3), 33–52.

Eden, C., & Greatbatch, R. J. (2008). Towards a mesoscale eddy closure. *Ocean Modelling*, *20*, 223-239. doi: 10.1016/j.ocemod.2007.09.002

Fox-Kemper, B., & Ferrari, R. (2008). Parameterization of mixed layer eddies. Part II: Prognosis and impact. *Journal of Physical Oceanography*, *38*(6), 1166 - 1179. doi: 10.1175/2007JPO3788.1

Fraser, A. D., Massom, R. A., Ohshima, K. I., Willmes, S., Kappes, P. J., Cartwright, J., & Porter-Smith, R. (2020). High-resolution mapping of circum-Antarctic landfast sea ice distribution, 2000–2018. *Earth System Science Data*, *12*(4), 2987–2999.

Fraser, A. D., Ohshima, K. I., Nihashi, S., Massom, R. A., Tamura, T., Nakata, K., ... Willmes, S. (2019). Landfast ice controls on sea-ice production in the Cape Darnley Polynya: A case study. *Remote Sensing of Environment*, *233*, 111315.

Gao, L., Zu, Y., Guo, G., & Hou, S. (2022). Recent changes and distribution of the newly-formed Cape Darnley Bottom Water, East Antarctica. *Deep Sea Research Part II: Topical Studies in Oceanography*, *201*, 105119.

Gent, P., Willebrand, J., McDougall, T., & McWilliams, J. (1995, 04). Parameterizing eddy-induced tracer transports in ocean circulation models. *Journal of Physical Oceanography*, *25*, 463-474. doi: 10.1175/1520-0485(1995)025⟨0463:PEITTI⟩2.0.CO;2

Gent, P. R., & McWilliams, J. C. (1990). Isopycnal mixing in ocean circulation models. *Journal of Physical Oceanography*, *20*(1), 150 - 155. doi: 10.1175/1520-0485(1990)020⟨0150:IMIOCM⟩2.0.CO;2

Gerdes, R., Köberle, C., & Willebrand, J. (1991, June). The influence of numerical advection schemes on the results of ocean general circulation models. *Climate Dynamics*, *5*(4), 211–226. doi: 10.1007/BF00210006

Green, J. S. A. (1970). Transfer properties of the large-scale eddies and the general circulation of the atmosphere. *Quarterly Journal of the Royal Meteorological Society*, *96*(408), 157-185. doi: 10.1002/qj.49709640802

Gudmundsson, G. H., Paolo, F. S., Adusumilli, S., & Fricker, H. A. (2019). Instantaneous Antarctic ice sheet mass loss driven by thinning ice shelves. *Geophysical Research Letters*, *46*(23), 13903–13909.

Haarsma, R. J., Roberts, M. J., Vidale, P. L., Senior, C. A., Bellucci, A., Bao, Q., ... others (2016). High Resolution Model Intercomparison Project (HighResMIP v1. 0) for CMIP6. *Geoscientific Model Development*, *9*(11), 4185–4208.

Hallberg, R. (2013, 12). Using a resolution function to regulate parameterizations of oceanic mesoscale eddy effects. *Ocean Modelling*, *72*, 92–103. doi: 10.1016/j.ocemod.2013.08.007

Hirano, D., Kitade, Y., Ohshima, K. I., & Fukamachi, Y. (2015). The role of turbulent mixing in the modified shelf water overflows that produce Cape Darnley Bottom Water. *Journal of Geophysical Research: Oceans*, *120*(2), 910–922.

Isachsen, P. E. (2011). Baroclinic instability and eddy tracer transport across sloping bottom topography: How well does a modified Eady model do in primitive equation simulations? *Ocean Modelling*, *39*(1), 183-199. doi: 10.1016/j.ocemod.2010.09.007

Jacobs, S. S., Hellmer, H., Doake, C. S. M., Jenkins, A., & Frolich, R. (1992). Melt-

ing of ice shelves and the mass balance of Antarctica. *Journal of Glaciology*, *38*(130), 375–387.

Jansen, M. F., Adcroft, A., Khani, S., & Kong, H. (2019). Toward an energetically consistent, resolution aware parameterization of ocean mesoscale eddies. *Journal of Advances in Modeling Earth Systems*, *11*(8), 2844-2860. doi: 10.1029/2019MS001750

Jansen, M. F., Adcroft, A. J., Hallberg, R., & Held, I. M. (2015). Parameterization of eddy fluxes based on a mesoscale energy budget. *Ocean Modelling*, *92*, 28-41. doi: 10.1016/j.ocemod.2015.05.007

Large, W. G., Danabasoglu, G., Doney, S. C., & McWilliams, J. C. (1997). Sensitivity to surface forcing and boundary layer mixing in a global ocean model: Annual-mean climatology. *Journal of Physical Oceanography*, *27*(11), 2418 - 2447. doi: 10.1175/1520-0485(1997)027⟨2418:STSFAB⟩2.0.CO;2

Legg, S., Briegleb, B., Chang, Y., Chassignet, E. P., Danabasoglu, G., Ezer, T., ... others (2009). Improving oceanic overflow representation in climate models: The gravity current entrainment climate process team. *Bulletin of the American Meteorological Society*, *90*(5), 657–670.

Leith, C. (1996). Stochastic models of chaotic systems. *Physica D: Nonlinear Phenomena*, *98*(2), 481-491. (Nonlinear Phenomena in Ocean Dynamics) doi: https://doi.org/10.1016/0167-2789(96)00107-8

Losch, M., Menemenlis, D., Campin, J.-M., Heimbach, P., & Hill, C. (2010). On the formulation of sea-ice models. Part 1: Effects of different solver implementations and parameterizations. *Ocean Modelling*, *33*(1-2), 129–144.

Mack, S. L., Dinniman, M. S., Klinck, J. M., McGillicuddy Jr, D. J., & Padman, L. (2019). Modeling ocean eddies on Antarctica's cold water continental shelves and their effects on ice shelf basal melting. *Journal of Geophysical Research: Oceans*, *124*(7), 5067–5084.

Mak, J., Maddison, J. R., Marshall, D. P., & Munday, D. R. (2018). Implementation of a geometrically informed and energetically constrained mesoscale eddy parameterization in an ocean circulation model. *Journal of Physical Oceanography*, *48*(10), 2363 - 2382. doi: 10.1175/JPO-D-18-0017.1

Mak, J., Maddison, J. R., Marshall, D. P., Ruan, X., Wang, Y., & Yeow, L. (2023). Scale-awareness in an eddy energy constrained mesoscale eddy parameterization. *Journal of Advances in Modeling Earth Systems*, *15*(12), e2023MS003886.

Manucharyan, G. E., & Isachsen, P. E. (2019). Critical role of continental slopes in halocline and eddy dynamics of the Ekman-driven Beaufort Gyre. *Journal of Geophysical Research: Oceans*, *124*(4), 2679-2696. doi: 10.1029/2018JC014624

Marshall, D. P., Maddison, J. R., & Berloff, P. S. (2012). A framework for parameterizing eddy potential vorticity fluxes. *Journal of Physical Oceanography*, *42*(4), 539–557. doi: 10.1175/JPO-D-11-048.1

Marshall, J., Adcroft, A., Hill, C., Perelman, L., & Heisey, C. (1997). A finite-volume, incompressible Navier Stokes model for studies of the ocean on parallel computers. *Journal of Geophysical Research: Oceans*, *102*(C3), 5753-5766. doi: 10.1029/96JC02775

McDougall, T. J., Jackett, D. R., Wright, D. G., & Feistel, R. (2003). Accurate and computationally efficient algorithms for potential temperature and density of seawater. *Journal of Atmospheric and Oceanic Technology*, *20*(5), 730 - 741. doi: 10.1175/1520-0426(2003)20⟨730:AACEAF⟩2.0.CO;2

Mechoso, C. R. (1980). Baroclinic instability of flows along sloping boundaries. *Journal of Atmospheric Sciences*, *37*(6), 1393 - 1399. doi: 10.1175/1520-0469(1980)037⟨1393:BIOFAS⟩2.0.CO;2

Mensah, V. (2021). *MITgcm model setup and output for "Dense water downslope flow and AABW production in a numerical model: sensitivity to horizontal and*

vertical resolution in the region off Cape Darnley Polynya [configuration]". doi: https://doi.org/10.5281/zenodo.4898376

Mensah, V., Nakayama, Y., Fujii, M., Nogi, Y., & Ohshima, K. I. (2021). Dense water downslope flow and AABW production in a numerical model: Sensitivity to horizontal and vertical resolution in the region off Cape Darnley polynya. *Ocean Modelling*, *165*, 101843.

MITgcm Group. (2025). *User manual.* `https://mitgcm.readthedocs.io/en/latest/`. (Last accessed: 2025-03-25)

Mizuta, G., Fukamachi, Y., Simizu, D., Matsumura, Y., Kitade, Y., Hirano, D., ... Ohshima, K. I. (2021). Seasonal evolution of Cape Darnley Bottom Water revealed by mooring measurements. *Frontiers in Marine Science*, *8*, 657119.

Mizuta, G., Ohshima, K. I., Takatsuka, T., Kitade, Y., Fujii, M., Nakayama, Y., & Ikehara, M. (2024). Circulation and production of Cape Darnley Bottom Water on the continental slope off the Cape Darnley polynya, East Antarctica. *Deep Sea Research Part I: Oceanographic Research Papers*, *211*, 104362.

Morrison, A. K., Hogg, A. M., England, M. H., & Spence, P. (2020). Warm circumpolar deep water transport toward Antarctica driven by local dense water export in canyons. *Science Advances*, *6*(18), eaav2516. doi: 10.1126/sciadv.aav2516

Nakayama, Y., Malyarenko, A., Zhang, H., Wang, O., Auger, M., Nie, Y., ... Menemenlis, D. (2024). Evaluation of MITgcm-based ocean reanalyses for the Southern Ocean. *Geoscientific Model Development*, *17*(23), 8613–8638. doi: https://doi.org/10.5194/gmd-17-8613-2024,2024

Nakayama, Y., Ohshima, K. I., Matsumura, Y., Fukamachi, Y., & Hasumi, H. (2014). A numerical investigation of formation and variability of Antarctic Bottom Water off Cape Darnley, East Antarctica. *Journal of Physical Oceanography*, *44*(11), 2921 - 2937. doi: 10.1175/JPO-D-14-0069.1

Nummelin, A., & Isachsen, P. E. (2024). Parameterizing mesoscale eddy buoyancy transport over sloping topography. *Journal of Advances in Modeling Earth Systems*, *16*(3), e2023MS003806. doi: https://doi.org/10.1029/2023MS003806

Ohshima, K. I., Fukamachi, Y., Ito, M., Nakata, K., Simizu, D., Ono, K., ... Tamura, T. (2022). Dominant frazil ice production in the Cape Darnley polynya leading to Antarctic Bottom Water formation. *Science advances*, *8*(42), eadc9174.

Ohshima, K. I., Fukamachi, Y., Williams, G. D., Nihashi, S., Roquet, F., Kitade, Y., ... others (2013). Antarctic Bottom Water production by intense sea-ice formation in the Cape Darnley polynya. *Nature Geoscience*, *6*(3), 235–240.

Phillips, N. A. (1954). Energy transformations and meridional circulations associated with simple baroclinic waves in a two-level, quasi-geostrophic model. *Tellus*, *6*(3), 274–286.

Pritchard, H., Ligtenberg, S., Fricker, H., Vaughan, D., Van den Broeke, M., & Padman, L. (2012, 04). Antarctic ice-sheet loss driven by basal melting of ice shelves. *Nature*, *484*, 502-5. doi: 10.1038/nature10968

Redi, M. H. (1982). Oceanic isopycnal mixing by coordinate rotation. *Journal of Physical Oceanography*, *12*(10), 1154 - 1158. doi: 10.1175/1520-0485(1982)012⟨1154:OIMBCR⟩2.0.CO;2

Shepherd, A., Ivins, E., Rignot, E., Smith, B., Van Den Broeke, M., Velicogna, I., ... others (2018). E., 2018. Mass balance of the Antarctic Ice Sheet from 1992 to 2017. *Nature*, *558*, 219–222.

Shimada, K., Aoki, S., & Ohshima, K. I. (2017). Creation of a gridded dataset for the Southern Ocean with a topographic constraint scheme. *Journal of Atmospheric and Oceanic Technology*, *34*(3), 511–532.

Si, Y., Stewart, A. L., & Eisenman, I. (2023). Heat transport across the Antarctic Slope Front controlled by cross-slope salinity gradients. *Science Advances*, *9*(18), eadd7049. doi: 10.1126/sciadv.add7049

Sterl, M. F., LaCasce, J. H., Groeskamp, S., Nummelin, A., Isachsen, P. E., & Baatsen, M. L. J. (2024). Suppression of mesoscale eddy mixing by topographic PV gradients. *Journal of Physical Oceanography*. doi: 10.1175/JPO-D-23-0142.1

Stewart, A., & Thompson, A. (2015, 12). Eddy-mediated transport of warm circumpolar deep water across the Antarctic shelf break. *Geophysical Research Letters*, *42*. doi: 10.1002/2014GL062281

Stewart, A., & Thompson, A. (2016, 10). Eddy generation and jet formation via dense water outflows across the Antarctic continental slope. *Journal of Physical Oceanography*, *46*. doi: 10.1175/JPO-D-16-0145.1

Stewart, A. L. (2021). Mesoscale, tidal, and seasonal/interannual drivers of the Weddell Sea overturning circulation. *Journal of Physical Oceanography*, *51*(12), 3695 - 3722. doi: 10.1175/JPO-D-20-0320.1

Stewart, A. L., & Thompson, A. F. (2013). Connecting Antarctic cross-slope exchange with Southern Ocean overturning. *Journal of Physical Oceanography*, *43*(7), 1453 - 1471. doi: 10.1175/JPO-D-12-0205.1

St-Laurent, P., Klinck, J. M., & Dinniman, M. S. (2013). On the role of coastal troughs in the circulation of warm circumpolar deep water on Antarctic shelves. *Journal of Physical Oceanography*, *43*(1), 51 - 64. doi: 10.1175/JPO-D-11-0237.1

Stone, P. H. (1972). A simplified radiative-dynamical model for the static stability of rotating atmospheres. *Journal of Atmospheric Sciences*, *29*(3), 405 - 418. doi: 10.1175/1520-0469(1972)029⟨0405:ASRDMF⟩2.0.CO;2

Thompson, A., Stewart, A., Spence, P., & Heywood, K. (2018, 11). The Antarctic Slope Current in a changing climate. *Reviews of Geophysics*, *56*. doi: 10.1029/2018RG000624

van Westen, R. M., & Dijkstra, H. A. (2021). Ocean eddies strongly affect global mean sea-level projections. *Science Advances*, *7*(15), eabf1674.

Visbeck, M., Marshall, J., Haine, T., & Spall, M. (1997). Specification of eddy transfer coefficients in coarse-resolution ocean circulation models. *Journal of Physical Oceanography*, *27*(3), 381 - 402. doi: 10.1175/1520-0485(1997)027⟨0381:SOETCI⟩2.0.CO;2

Wang, Y., & Stewart, A. L. (2020). Scalings for eddy buoyancy transfer across continental slopes under retrograde winds. *Ocean Modelling*, *147*, 101579. doi: 10.1016/j.ocemod.2020.101579

Wei, H., & Wang, Y. (2021). Full-depth scalings for isopycnal eddy mixing across continental slopes under upwelling-favorable winds. *Journal of Advances in Modeling Earth Systems*, *13*(6), e2021MS002498. doi: 10.1029/2021MS002498

Wei, H., Wang, Y., & Mak, J. (2024). Parameterizing eddy buoyancy fluxes across prograde shelf/slope fronts using a slope-aware GEOMETRIC closure. *Journal of Physical Oceanography*, *54*(2), 359 - 377. Retrieved from `https://journals.ametsoc.org/view/journals/phoc/54/2/JPO-D-23-0152.1.xml` doi: 10.1175/JPO-D-23-0152.1

Wei, H., Wang, Y., Stewart, A. L., & Mak, J. (2022). Scalings for eddy buoyancy fluxes across prograde shelf/slope fronts. *Journal of Advances in Modeling Earth Systems*, *14*(12), e2022MS003229. (e2022MS003229 2022MS003229) doi: 10.1029/2022MS003229

Winton, M., Hallberg, R., & Gnanadesikan, A. (1998). Simulation of density-driven frictional downslope flow in z-coordinate ocean models. *Journal of Physical Oceanography*, *28*(11), 2163 - 2174. doi: 10.1175/1520-0485(1998)028⟨2163:SODDFD⟩2.0.CO;2

Wong, A. P., & Riser, S. C. (2013). Modified shelf water on the continental slope north of Mac Robertson Land, East Antarctica. *Geophysical Research Letters*, *40*(23), 6186–6190.

Zhang, H., Menemenlis, D., & Fenty, I. (2018). *ECCO LLC270 ocean-ice state estimate.* `http://hdl.handle.net/1721.1/119821`.